QuaDRiGa: A 3-D Multi-Cell Channel Model With Time Evolution for Enabling Virtual Field Trials

Stephan Jaeckel, *Member, IEEE*, Leszek Raschkowski, Kai Börner, *Student Member, IEEE*, and Lars Thiele, *Member, IEEE*

***Abstract*—Channel models are important tools to evaluate the performance of new concepts in mobile communications. However, there is a tradeoff between complexity and accuracy. In this paper, we extend the popular Wireless World Initiative for New Radio (WINNER) channel model with new features to make it as realistic as possible. Our approach enables more realistic evaluation results at an early stage of algorithm development. The new model supports 3-D propagation, 3-D antenna patterns, time evolving channel traces of arbitrary length, scenario transitions and variable terminal speeds. We validated the model by measurements in a coherent LTE advanced testbed in downtown Berlin, Germany. We then reproduced the same scenario in the model and compared several channel parameters (delay spread, path gain, K-factor, geometry factor and capacity). The results match very well and we can accurately predict the performance for an urban macro-cell setup with commercial high-gain antennas. At the same time, the computational complexity does not increase significantly and we can use all existing WINNER parameter tables. These artificial channels, having equivalent characteristics as measured data, enable virtual field trials long before prototypes are available.**

***Index Terms*—Coherent multi-cell measurements, multiple-input multiple-output (MIMO) channel, MIMO systems, modeling, parameterization, radio propagation, spatial channel model (SCM), validation, Wireless World Initiative for New Radio (WINNER).**

I. Introduction

THERE are several ways to validate new concepts in mobile communication systems. Ideally, everything would be tested using real-time prototypes. However, this is only possible after the standardization and product development stages. In the research stage, i.e., before standardization and product development, early field trials are often helpful to promote new approaches towards standardization. However, the value of such early trials is rather limited from a performance evaluation point of view. Therefore, they are usually combined with simulation studies taking the channel and interference statistics into account. Channel models such as the 3GPP spatial channel model (SCM) [1], the Wireless World Initiative for New Radio (WINNER) model [2], [3] and the European Cooperation in Science and Technology (COST) 273/2100 channel model [4], [5] are reliable tools for such studies.

The 3GPP SCM [1], its extensions [6], [7] and the WINNER model [2] are based on a 2-D modeling approach. However, Shafi *et al.* [8] pointed out the importance of a 3-D extension when studying the effects of cross-polarized antennas on the multiple-input multiple-output (MIMO) capacity. This was taken up in the WINNER+ project where the parameter tables were completed with the elevation component [3]. However, a 3-D WINNER+ channel model is not available. Meanwhile, 3-D propagation was incorporated into other models such as the COST model [5] or mobile-to-mobile propagation models [9]. They share similar ideas which we use in this paper to incorporate 3-D propagation and 3-D antenna patterns into an extension of the WINNER model.

Another prerequisite for "virtual field trials" is the continuous time evolution of channel traces. Xiao *et al.* [6] added short-term time evolution to the SCM, that was incorporated into an official SCM extension [7]. The idea is to calculate the position of the last-bounce scatterers (LBSs) based on the arrival angles of individual multipath components. Then, when the mobile terminal (MT) is moving, the arrival angles, delays, and phases are updated using geometrical calculations. However, the WINNER II model did not incorporate this technique. Hence, the WINNER model does not support time evolution beyond the scope of a few milliseconds, restricting the mobility of the MTs to a few meters.

The COST model [4] incorporates time evolution by introducing groups of randomly placed scattering clusters that fade in and out depending on the MT position. However, despite the effort that was made to parameterize the model [10], [11], it still lacks sufficient parameters in many interesting scenarios. Czink *et al.* [12] introduced a simplified method that fades the clusters in and out over time. The cluster parameters were extracted from measurements, and the model is well suited for link-level simulations. However, this "random cluster model" cannot be used for system-level scenarios, because it does not include geometry-based deployments like in the SCM, COST, and WINNER models. Nevertheless, the ideas presented by [12] led to more research on the birth/death probability as well as the lifetime of individual scattering clusters [13]. Wang *et al.* [14] then proposed a model for nonstationary channels that allows the scattering clusters to be mobile.

Manuscript received February 08, 2013; revised December 19, 2013; accepted February 19, 2014. Date of publication March 06, 2014; date of current version May 29, 2014. This work was supported by the German Federal Ministry of Economics and Technology (BMWi) in the national collaborative project IntelliSpektrum under contract 01ME11024, by the European Space Research and Technology Centre (ESTEC) under contract AO/1-5985/09/08/NL/LvH (Acronym: MIMOSA), and by the German Federal Ministry of Education and Research (BMBF) under contract 01BU0631 (Acronym: EASY-C).

The authors are with the Fraunhofer Institute for Telecommunications, Heinrich Hertz Institute, D-10587 Berlin, Germany (e-mail: stephan.jaeckel@ieee.org).

Digital Object Identifier 10.1109/TAP.2014.2310220

0018-926X © 2014 IEEE. Translations and content mining are permitted for academic research only. Personal use is also permitted, but republication/redistribution requires IEEE permission. See http://www.ieee.org/publications_standards/publications/rights/index.html for more information.

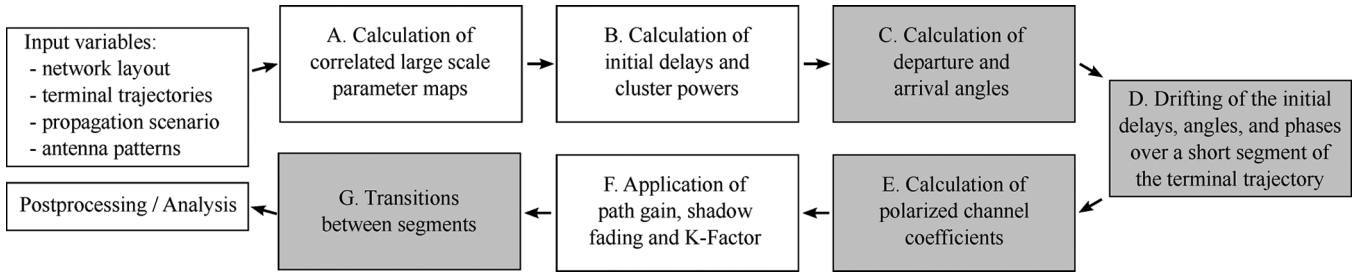

Fig. 1. Steps for the calculation of time-evolving channel coefficients. Compared to the WINNER model, changes were made in the gray shaded boxes.

In our extension of the WINNER model, we incorporate time evolution based on the ideas presented in [6] and [7]. We introduce the new model under the acronym "QuaDRiGa"—Quasi Deterministic Radio Channel Generator. A reference implementation in MATLAB is available as open source [15]. Our approach consists of two steps: A stochastic part generates large-scale parameters (LSPs) and calculates random 3-D positions of scattering clusters. We assume that the base stations (BSs) are fixed and the MTs are moving. In this case, scattering clusters are fixed as well and the time evolution of the radio channel is deterministic. Different positions of the MT lead to different arrival angles, delays, and phases for each multipath component (MPC). Longer sequences are generated by transitions between channel traces from consecutive initializations of the model. This allows the MTs to traverse different scenarios, e.g., move from indoors to outdoors.

We validated the model by measurements in downtown Berlin, Germany. We extracted several single-link and multi-link parameters and compared them with those obtained from the channel model. The results agree very well. Remaining deviations can be explained by some specific characteristics of our measurement system. In this way, we show that it is possible to emulate a real-world scenario accurately.

The paper is organized as follows. Section II describes the model in detail. Section III reports on the measurements. Section IV then compares the results from both model and measurement. Section V concludes the paper.

II. Description of the Channel Model

Our modeling approach is an extension of the WINNER model [2]. Fig. 1 gives an overview of the modeling steps. The user needs to configure the network layout (i.e., the positions of the BSs, antenna configurations, downtilts), the positions and trajectories of the MTs, and the propagation scenarios. The channel coefficients are then calculated in seven steps, which are described in detail in Sections II-A to II-G. Major extensions concerning 3-D propagation are made in steps C and D. Time evolution is incorporated in steps D and G, and a new 3-D model of the polarization [16] is introduced in step E. In order to integrate these extensions, some changes are made in the other parts of the model as well.

Time evolution requires a more detailed description of the mobility of the terminals. This is done by assigning tracks, i.e., ordered lists of positions, to each MT. Realistic scenarios may include accelerations, decelerations, and MTs with different speeds, e.g., pedestrian and vehicular users. However, to minimize the computational overhead and memory requirements, we calculate channel coefficients at a constant sample rate that fulfills the sampling theorem

$$f_T \geq 2B_D = 4\max|\Delta f_D| = 4\frac{\max|v|}{\lambda_c} \tag{1}$$

where B_D is the width of the Doppler spectrum, Δf_D is the maximum frequency change due to the velocity v, and λ_c is the carrier wavelength. Thus, the appropriate sampling rate is proportional to the maximum speed of the MT. Since it is sometimes useful to examine algorithms at different speeds, it is unfortunate to fix the sampling rate in advance as the speed is then fixed as well. To overcome this problem, we calculate channel coefficients at fixed positions with a sampling rate f_S measured in samples per meter. In its normalized form, it is known as sample density (SD). A time-series for arbitrary or varying speeds is then obtained by interpolating the coefficients in a postprocessing step:

$$f_S = \frac{f_T}{\max|v|} \geq \frac{4}{\lambda_c} \tag{2}$$

$$\mathrm{SD} = \frac{f_S}{\lambda_c/2} \geq 2. \tag{3}$$

Longer time-evolving channel sequences need to consider the birth and death of scattering clusters as well as transitions between different propagation environments. We address this by splitting the MT trajectory into *segments*. A segment can be seen as an interval in which the LSPs do not change considerably and where the channel keeps its wide sense stationary (WSS) properties. Thus, the length of a segment depends on the decorrelation distances of the LSPs. We propose to limit the segment length to the average decorrelation distance. In the WINNER urban macro-cell (UMa) scenario, this would be 22 m for line-of-sight (LOS) and 48 m for non-line-of-sight (NLOS) propagation. Channel traces are then generated independently for each segment. In Section II-G we combine those individual traces into a longer sequence that includes the birth and death of scattering clusters.

A. Correlated Large-Scale Parameter Maps

The positions of the scattering clusters are based on seven large-scale parameters (LSPs):

1) RMS delay spread (DS).
2) Ricean K-factor (KF).
3) Shadow fading (SF).
4) Azimuth spread of departure (ASD).
5) Azimuth spread of arrival (ASA).
6) Elevation spread of departure (ESD).
7) Elevation spread of arrival (ESA).

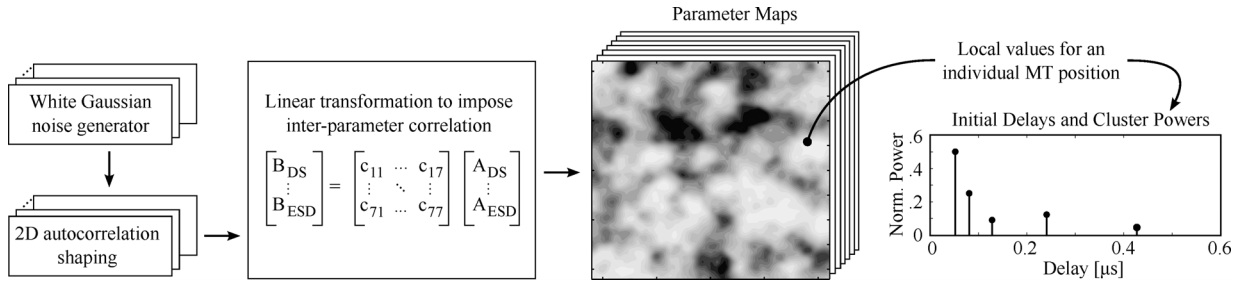

Fig. 2. Principle of the generation of channel coefficients based on correlated LSPs.

Their distribution properties are directly obtained from measurement data (e.g., [17]–[19], [3], [2]). If some MTs or segments are close to each other, their LSPs will be correlated and they will experience similar propagation conditions. This is modeled by means of 2-D maps, as illustrated in Fig. 2. Our method for generating these maps is adopted from [20]. The maps are initialized with values obtained from an independent and identically distributed (i.i.d.) zero-mean Gaussian random process with desired variance. The pixels are then subsequently filtered to obtain the desired autocorrelation function, i.e., a decaying exponential function with a specific decorrelation distance. In contrast to [20], we filter the maps in the diagonal direction as well to get a smooth evolution of the values along the MT trajectory. Advanced methods going beyond our approach for generating such maps are discussed in [21]. Once the maps are generated, initial LSPs for each segment are obtained by interpolating the maps to match the exact position of the MT.

B. Initial Delays and Cluster Powers

Initial delays are drawn randomly from a scenario-dependent delay distribution as

$$\tau_l^{[1]} = -r_\tau \sigma_\tau \ln(X_l) \tag{4}$$

where $X_l \sim \mathrm{uni}(0,1)$ is an uniformly distributed random variable having values between 0 and 1, σ_τ is the initial DS from the map and r_τ is a proportionality factor (see [2]). The term r_τ was introduced in [1] because σ_τ is influenced by both the delays τ_l and the powers P_l; r_τ is usually calculated from measurement data. Next, the delays are normalized such that the first delay is zero and then they are sorted:

$$\tau_l^{[2]} = \mathrm{sort}\left\{\tau_l^{[1]} - \min\left(\tau_l^{[1]}\right)\right\}. \tag{5}$$

The NLOS cluster powers are drawn from a single slope exponential power-delay profile (PDP) depending on the DS σ_τ and a random component $Z_l \sim \mathcal{N}(0,\zeta^2)$ [2]. The term ζ is a scenario-dependent coefficient emulating an additional shadowing process. It is obtained from measurements:

$$P_l^{[1]} = \exp\left(-\tau_l \frac{r_\tau - 1}{r_\tau \sigma_\tau}\right) \cdot 10^{\frac{-Z_l}{10}}. \tag{6}$$

The power of the first cluster is further scaled according to the initial KF from the map and cluster powers are normalized so that their sum power is one:

$$P_1^{[2]} = K \sum_{l=2}^{L} P_l^{[1]}; P_{2\ldots l}^{[2]} = P_{2\ldots l}^{[1]} \text{ and } P_l = P_l^{[2]} \Big/ \sum_{l=1}^{L} P_l^{[2]}. \tag{7}$$

In the last step, we correct the influence of the KF on the DS, which has changed due to the scaling. The DS after applying (7) is calculated using (41) from Section III-C with P_i set to one. This value is denoted as $\sigma_\tau^{[\mathrm{actual}]}$. With σ_τ being the initial DS from the map, cluster delays note

$$\tau_l = \frac{\sigma_\tau}{\sigma_\tau^{[\mathrm{actual}]}} \cdot \tau_l^{[2]}. \tag{8}$$

C. Departure and Arrival Angles

We calculate four angles for each cluster. In addition to the azimuth angle of departure (AoD, ϕ^d) and the azimuth angle of arrival (AoA, ϕ^a) used in the 2-D WINNER model, we also calculate the elevation angle of departure (EoD, θ^d) and the elevation angle of arrival (EoA, θ^a). The angles share the same calculation method but have different angular spreads σ_ϕ. Hence, we use σ_ϕ representative for $\sigma_{\phi^a}, \sigma_{\phi^d}, \sigma_{\theta^a}, \sigma_{\theta^d}$ in the following. We assume that the power angular spectrum of all clusters follows a wrapped Gaussian distribution [2], [22]:

$$P(\phi) = \frac{1}{\sigma_\phi \sqrt{2\pi}} \exp\left(\frac{-\phi^2}{2\sigma_\phi^2}\right). \tag{9}$$

The wrapping is applied later by (12) when the discrete cluster angles are drawn from the statistics. Since the above formula assumes a continuous spectrum, whereas the channel model uses discrete paths, we need to correct the variance by a function $C_\phi(L,K)$. This function ensures that the input variance σ_ϕ is correctly reflected in the generated angles. It is derived in the Appendix.

We obtain the angles ϕ_l by first normalizing the power angular spectrum so that its maximum has unit power. We can thus omit the scaling factor $1/(\sigma_\phi\sqrt{2\pi})$. We also normalize the path powers P_l (7) so that the strongest peak with unit power corresponds to an angle $\phi = 0$. All other paths get relative departure or arrival angles depending on their power:

$$\phi_l^{[1]} = \frac{\sigma_\phi}{C_\phi(L,K)} \cdot \sqrt{-2 \cdot \ln(P_l/\max(P_l))}. \tag{10}$$

The value σ_ϕ is measured in radians here. Next, we create two random variables, X_l and Y_l, where $X_l \sim \{-1,1\}$ is the positive or negative sign and $Y_l \sim \mathcal{N}(0, 0.01 \cdot \sigma_\phi^2)$ introduces a random variation on the angle. Then we calculate

$$\phi_l^{[2]} = X_l \cdot \phi_l^{[1]} + Y_l. \tag{11}$$

TABLE I
OFFSET ANGLE OF THE mTH SUB-PATH FROM [2]

Sub-path m	Offset angle $\hat{\phi}_m$ (degrees)	Sub-path m	Offset angle $\hat{\phi}_m$ (degrees)
1,2	± 0.0447	11,12	± 0.6797
3,4	± 0.1413	13,14	± 0.8844
5,6	± 0.2492	15,16	± 1.1481
7,8	± 0.3715	17,18	± 1.5195
9,10	± 0.5129	19,20	± 2.1551

If the power P_l of a path is small compared with the strongest peak, its angle $\phi_l^{[2]}$ might exceed $\pm\pi$. In this case, we wrap it around the unit circle by a modulo operation:

$$\phi_l^{[3]} = \left(\phi_l^{[2]} + \pi \bmod 2\pi\right) - \pi. \tag{12}$$

In case of elevation spreads, the possible range of elevation angles goes from $-\pi/2$ to $\pi/2$. In this case, we have to correct values of $\phi_l^{[3]}$ outside of this range:

$$\phi_l^{[4]} = \begin{cases} \phi_l^{[3]}, & \text{for el. } \left|\phi_l^{[3]}\right| < \frac{\pi}{2} \text{ and all az. angles} \\ \pi - \phi_l^{[3]}, & \text{for elevation } \phi_l^{[3]} > \frac{\pi}{2} \\ \phi_l^{[3]} - \pi, & \text{for elevation } \phi_l^{[3]} < -\frac{\pi}{2}. \end{cases} \tag{13}$$

The positions of the transmitter (Tx) and receiver (Rx) are deterministic, and so are the angles of the LOS component. We correct the values of the angles to incorporate this position:

$$\phi_l^{[5]} = \phi_l^{[4]} - \phi_1^{[4]} + \phi^{LOS}. \tag{14}$$

Finally, the NLOS cluster-paths are split into 20 sub-paths to emulate intra-cluster angular spreads. The LOS path has no sub-paths.

$$\phi_{l,m} = \phi_l^{[5]} + c_\phi \cdot \hat{\phi}_m, \quad \text{for } l > 1. \tag{15}$$

m is the sub-path index, c_ϕ is the scenario-dependent cluster-wise RMS angular spread and $\hat{\phi}$ is the offset angle of the mth sub-path from Table I. Furthermore, each of the 20 angle pairs $(\theta_{l,m}^d, \phi_{l,m}^d)$ at the Tx gets coupled with a random angle pair $(\theta_{l,m}^a, \phi_{l,m}^a)$ at the Rx (see [2]).

D. Drifting

After cluster-delays, powers, and angles are known for the initial position, we update their values for each snapshot of the segment. Thus, we get an evolution of the parameters over a short time interval. Drifting for 2-D propagation was already introduced in an extension of the SCM [7]. However, it was not incorporated into the WINNER model and no evaluation was reported. Here, we extend this idea towards 3-D propagation to incorporate time evolution into the new model.

Besides the parameters from steps B and C, drifting requires the exact position of each antenna element. At the MT, element positions need to be updated for each snapshot with respect to the MT orientation. The following calculations are then done element-wise. The indices r, t, l, m, s denote the index of the Rx antenna element (r) and the Tx antenna element (t), the cluster number (l), the sub-path number (m), and the snapshot number (s) within the current segment, respectively.

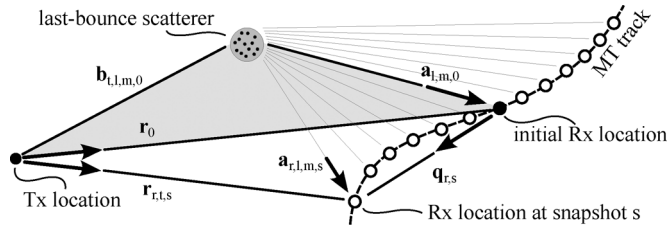

Fig. 3. Illustration of the calculation of the scatterer positions and updates of the arrival angles.

a) NLOS Drifting: We keep the scatterer positions fixed for the time it takes a MT to move through a segment. Hence, the angles (θ^d, ϕ^d) seen from the BS do not change except for the LOS angle, which is treated separately. Based on this assumption, the angles (θ^a, ϕ^a) as well as the path delay only change with respect to the last-bounce scatterer (LBS). Hence, if the BS array size is small compared to the BS-MT distance, it is sufficient to consider only a single scatterer (the LBS) for the NLOS paths.

We calculate the position of the LBS from the initial arrival angles and the cluster delays. Then we update the angles and path lengths between the LBS and the terminal for each snapshot on the track. This is done for each antenna element separately. Fig. 3 illustrates the angles and their relations. The first delay is always zero due to (5). Hence, we calculate the total length of the lth path as

$$d_l = \tau_l \cdot c + |\mathbf{r}_0| \tag{16}$$

where $|\mathbf{r}_0|$ is the distance between the Tx and the initial Rx location, and c is the speed of light. We assume that all sub-paths have the same delay and thus the same path length. However, each sub-path has different arrival angles $(\theta_{l,m}^a, \phi_{l,m}^a)$. We transform those angles into Cartesian coordinates and obtain

$$\hat{\mathbf{a}}_{l,m,0} = \frac{\mathbf{a}_{l,m,0}}{|\mathbf{a}_{l,m,0}|} = \begin{pmatrix} \cos\phi_{l,m}^a \cdot \cos\theta_{l,m}^a \\ \sin\phi_{l,m}^a \cdot \cos\theta_{l,m}^a \\ \sin\theta_{l,m}^a \end{pmatrix}. \tag{17}$$

We approximate the drifting at the MT using only a single reflection. Hence, Tx, Rx, and LBS form a triangle. Since we know d_l, $\mathbf{r}_0$, and $\hat{\mathbf{a}}_{l,m,0}$, we can apply the cosine theorem to calculate the distance $|\mathbf{a}_{l,m,0}|$ between the Rx and LBS[1]:

$$\begin{aligned} b_{l,m,0}^2 &= |\mathbf{r}_0|^2 + |\mathbf{a}_{l,m,0}|^2 \\ &\quad - 2|\mathbf{r}_0||\mathbf{a}_{l,m,0}|\cos\beta_{l,m,0} \\ (d_l - |\mathbf{a}_{l,m,0}|)^2 &= |\mathbf{r}_0|^2 + |\mathbf{a}_{l,m,0}|^2 + 2|\mathbf{a}_{l,m,0}|\mathbf{r}_0^T\hat{\mathbf{a}}_{l,m,0} \\ |\mathbf{a}_{l,m,0}| &= \frac{d_l^2 - |\mathbf{r}_0|^2}{2\cdot(d_l + \mathbf{r}_0^T\hat{\mathbf{a}}_{l,m,0})}. \end{aligned} \tag{18}$$

Now we can calculate the vector $\mathbf{a}_{r,l,m,s}$ for the Rx antenna element r at snapshot s. The element position includes the orientation of the antenna array with respect to the moving direc-

[1]We substitute $\cos\beta_{l,m,0}$ with $-\mathbf{r}_0^T\hat{\mathbf{a}}_{l,m,0}/|\mathbf{r}_0|$ since we are at the Rx position looking towards the Tx.

tion of the Rx. Hence, the vector $\mathbf{q}_{r,s}$ points from the initial Rx location to the rth antenna element at snapshot s:

$$\mathbf{a}_{r,l,m,s} = \mathbf{a}_{l,m,0} - \mathbf{q}_{r,s}. \tag{19}$$

We obtain an update of the arrival angles by transforming $\mathbf{a}_{r,l,m,s}$ back to spherical coordinates:

$$\phi^a_{r,l,m,s} = \arctan_2\{a_{r,l,m,s,y}, a_{r,l,m,s,x}\} \tag{20}$$

$$\theta^a_{r,l,m,s} = \arcsin\left\{\frac{a_{r,l,m,s,z}}{|\mathbf{a}_{r,l,m,s}|}\right\}. \tag{21}$$

Since we assume a static scattering environment, we use the same departure angles for all Tx elements. The phases and path delays, however, depend on the total path length $d_{r,t,l,m,s}$. To obtain this value, we calculate the vector $\mathbf{b}_{t,l,m,0}$ from the vectors $\mathbf{r}_{r,t,s}$ and $\mathbf{a}_{r,l,m,s}$ at $r = s = 1$:

$$\mathbf{b}_{t,l,m,0} = \mathbf{r}_{1,t,1} + \mathbf{a}_{1,l,m,1} \tag{22}$$

$$d_{r,t,l,m,s} = |\mathbf{b}_{t,l,m,0}| + |\mathbf{a}_{r,l,m,s}|. \tag{23}$$

Finally, we calculate the phases ψ and path delays τ:

$$\psi_{r,t,l,m,s} = \frac{2\pi}{\lambda} \cdot (d_{r,t,l,m,s} \bmod \boldsymbol{\lambda}) \tag{24}$$

$$\tau_{r,t,l,s} = \frac{1}{20 \cdot c} \sum_{m=1}^{20} d_{r,t,l,m,s}. \tag{25}$$

b) LOS Drifting: The direct component is handled differently, since we have to update the angles at both the Tx and the Rx sides. We update the departure and arrival angles for each combination of Tx-Rx antenna elements based on the position of the element in 3-D coordinates:

$$\phi^d_{t,1,s} = \arctan_2\{r_{r,t,s,y}, r_{r,t,s,x}\} \tag{26}$$

$$\theta^d_{t,1,s} = \arcsin\left\{\frac{r_{r,t,s,z}}{|\mathbf{r}_{r,t,s}|}\right\} \tag{27}$$

$$\phi^a_{r,1,s} = \arctan_2\{-r_{r,t,s,y}, -r_{r,t,s,x}\} \tag{28}$$

$$\theta^a_{r,1,s} = \arcsin\left\{\frac{-r_{r,t,s,z}}{|\mathbf{r}_{r,t,s}|}\right\}. \tag{29}$$

The vector $\mathbf{r}_{r,t,s}$ points from the location of the Tx element t to the location of the Rx element r at snapshot s (see Fig. 3). The phases and delays are determined by the length of this vector and are calculated using (24) and (25) where $d_{r,t,l,m,s}$ is replaced by $|\mathbf{r}_{r,t,s}|$.

E. Polarized Channel Coefficients

Next, we combine antenna patterns, polarization, and phases to calculate initial channel coefficients for each snapshot of a segment. The antennas are defined by their 3-D polarimetric response $\mathbf{F}$ containing vertical and horizontal polarization in spherical coordinates [23]:

$$\mathbf{F}(\theta, \phi) = \begin{pmatrix} F_V(\theta, \phi) \\ F_H(\theta, \phi) \end{pmatrix}. \tag{30}$$

We read the directional antenna gains from both the Tx and Rx antennas using the previously calculated departure and arrival angles and calculate the coefficient

$$g^{[1]}_{r,t,l,m,s} = \mathbf{F}_r(\theta^a_{r,l,m,s}, \phi^a_{r,l,m,s})^T \cdot \mathbf{M} \cdot \mathbf{F}_t(\theta^d_{t,l,m,s}, \phi^d_{t,l,m,s}). \tag{31}$$

The polarization is changed along the propagation path. This is captured by the matrix $\mathbf{M}$. The SCM, WINNER, and COST models use random coefficients to handle polarization effects. However, in our separate publication [16], we discussed how this does not account for all effects contributing to the polarization state of a MIMO radio link. Thus, we proposed a method for calculating $\mathbf{M}$ based on linear transformations, which we use here as well.

Each MPC has a random initial phase ψ^0. Hence, by summing up the 20 sub-paths to get one path per cluster, we get a random cluster power. This is compensated by normalization where we first sum up the complex phases and then average the power over all S snapshots of the segment. We update the channel coefficients (31) as

$$\psi^+_{r,t,l,m,s} = \exp\left(-j\psi^0_{l,m} - j\psi_{r,t,l,m,s}\right) \tag{32}$$

$$g^{[2]}_{r,t,l,s} = \sqrt{\frac{P_l}{\beta}} \cdot \sum_{m=1}^{20} g^{[1]}_{r,t,l,m,s} \cdot \psi^+_{r,t,l,m,s} \tag{33}$$

$$\beta = \frac{1}{S} \sum_{s=1}^{S} \left(\sum_{m=1}^{20} \psi^+_{r,t,l,m,s}\right)^2 \tag{34}$$

where P_l is the initial power assigned to each cluster.

F. Path Gain, Shadow Fading and K-Factor

Now, we apply the path gain (PG), the SF, and the KF. Hata [24] presented a simple model for macro-cellular settings where the PG scales with the logarithm of the distance d (in units of meters) between BS and terminal:

$$\mathrm{PG}^{[\mathrm{dB}]} = -A \cdot 10 \log_{10} d_{[\mathrm{m}]} - B \tag{35}$$

where A and B are scenario-specific coefficients that are typically determined by measurements. The path gain exponent A often varies between values of 2 and 4, depending on the propagation conditions, the BS height, and other factors. Combining PG and SF results in the effective path gain $\mathrm{PG}^{[\mathrm{eff}]}$. The values for the SF and the KF are obtained from the LSP map by an interpolation of the surrounding pixels at the position of the sth snapshot. The KF at the initial position is already included due to the scaling in (7). Thus, we have to take this into account and scale the power accordingly:

$$\mathrm{PG}^{[\mathrm{eff}]}_s = \sqrt{10^{0.1\left(\mathrm{PG}^{[\mathrm{dB}]}_s + \mathrm{SF}^{[\mathrm{dB}]}_s\right)}} \cdot \sqrt{1 + P_1\left(\frac{K_s}{K_0} - 1\right)} \tag{36}$$

$$g_{r,t,l,s} = \mathrm{PG}^{[\mathrm{eff}]}_s \cdot \begin{cases} \sqrt{\frac{K_s}{K_0}} \cdot g^{[2]}_{r,t,l,s}, & \text{for } l = 1 \\ g^{[2]}_{r,t,l,s}, & \text{otherwise.} \end{cases} \tag{37}$$

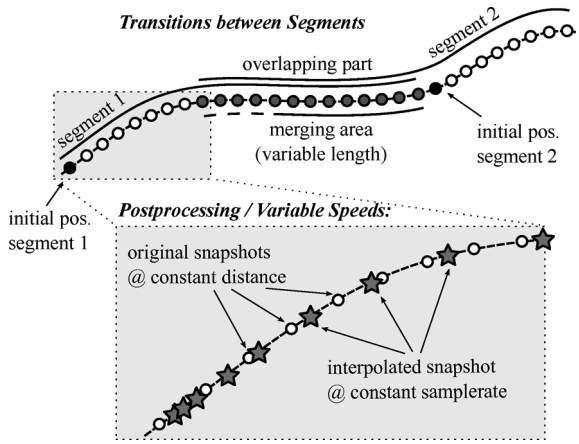

Fig. 4. Top: illustration of the overlapping area used for calculating the transitions between segments (step G), Bottom: illustration of the interpolation to obtain variable MT speeds (step H).

In the above equations, K_s and $\mathrm{SF}_s^{[\mathrm{dB}]}$ are the interpolated values for the KF and the SF from the map, K_0 is the KF at the initial position, $\mathrm{PG}_s^{[\mathrm{dB}]}$ is the path gain (without SF) at the MT position (35), and P_1 is the power of the LOS cluster (7).

G. Transitions Between Segments

The calculations in Sections II-B to II-F were done independently for each segment of the MT trajectory. Here, we combine those segments into a long, time-evolving sequence of channel coefficients. The idea comes from the WINNER II model [2]. However, it was neither implemented nor tested. Our implementation requires that parts of the segments are overlapping as depicted in the top of Fig. 4.

The lifetime of a scattering cluster is confined within the combined length of two adjacent segments. The power of clusters from the old segment is ramped down and the power of new clusters is ramped up within the overlapping region of the two segments. Hence, this process describes the birth and death of clusters along the trajectory. Outside the overlapping region, all clusters of the segment are active. We further split the overlapping region into subintervals to keep the computational overhead low. During each subinterval, one old cluster ramps down and one new cluster ramps up. We model the power ramps by a squared sine function:

$$w^{[\mathrm{sin}]} = \sin^2\left(\frac{\pi}{2} \cdot w^{[\mathrm{lin}]}\right). \tag{38}$$

Here, $w^{[\mathrm{lin}]}$ is the linear ramp ranging from 0 to 1, and $w^{[\mathrm{sin}]}$ is the corresponding sine-shaped ramp with a constant slope at the beginning and the end. This prevents inconsistencies at the edges of the subintervals. If both segments have a different number of clusters, the ramp is stretched over the whole overlapping area for clusters without a partner. For the LOS cluster, which is present in both segments, we adjust only power and phase.

Clusters need to be carefully matched to minimize the impact of the transition on the instantaneous values of the LSPs. For example, the DS increases if a cluster with a small delay ramps down and a similarly strong cluster with a large delay ramps up. Hence, the DS can fluctuate randomly within the overlapping region. To balance this out we pair clusters from both segments that minimize these fluctuations. This is done by determining the values of the DS before and after the transition. Then, we calculate a target DS for each subinterval. For example, if the old segment yields a DS of 200 ns and the new segment has 400 ns, then the target DS will be 220 ns for the first subinterval, 240 ns for the second and so on. Then we look for a combination of clusters that best matches the target DS for each subinterval.

H. Postprocessing/Variable Speeds

In the real world, MTs move at arbitrary speeds, including accelerations and decelerations. Provided that the sampling theorem is fulfilled, we can interpolate the channel coefficients to include such effects. This is illustrated in the bottom part of Fig. 4. The white dots represent the snapshots at a constant distance. However, the sample points (gray stars) can have unequal spacing, e.g., for an accelerated movement. Each sample point in the time domain (given in units of seconds) has a corresponding position on the MT trajectory (in units of meters). The amplitudes and phases of the channel coefficients are interpolated separately using cubic spline interpolation. The path delays are interpolated with a piecewise cubic hermite interpolating polynomial.

III. Validation Method

To validate the model, we used measurement data from our multi-cell testbed in downtown Berlin, Germany. Detailed information on the testbed is available in [25]–[28]. The same scenario (in terms of BS and MT positions) was replicated using the channel model. We extracted several large-scale parameters from both data sets and compared their distributions. Here, we describe the measurement and channel model setup as well as the metrics used for evaluating the data.

A. Measurement Setup

Our measurement setup replicated a small pre-commercial long-term evolution (LTE)-advanced scenario consisting of six sectors. All sectors were equipped with commercial Kathrein XPol panel antennas[2] with a half-power beam width of 60° in azimuth and 6° in elevation direction (polarization ±45°, 18 dBi gain). All sites were synchronized using GPS-disciplined Rubidium clocks that allowed phase-coherent operation in the same frequency band. Reference signals [29] consisting of 144 pilot tones for each BS served for coherently identifying up to six cells. Additional orthogonal sequences over four consecutive symbols allowed the identification of multiple antennas per cell.

At the Rx side, we used a customized terminal equipped with a pair of dipole-like antennas[3] (4 dBi gain). These antennas were mounted on the roof of a car and slanted by ±45°. The terminal was synchronized over the air to simplify the measurement procedure and to eliminate additional calibration steps. The system automatically adjusted the multi-cell channel impulse response (CIR) within the 4.7 μs guard interval of the underlying orthogonal frequency-division multiplexing (OFDM) system which removed the mean multi-cell delay from the data. The MT detected the reference signals and converted them into an Ethernet

[2]Type No. 800 10541

[3]HUBER+SUHNER SWA 2459/360/4/45/V; Type: 1399.17.0040

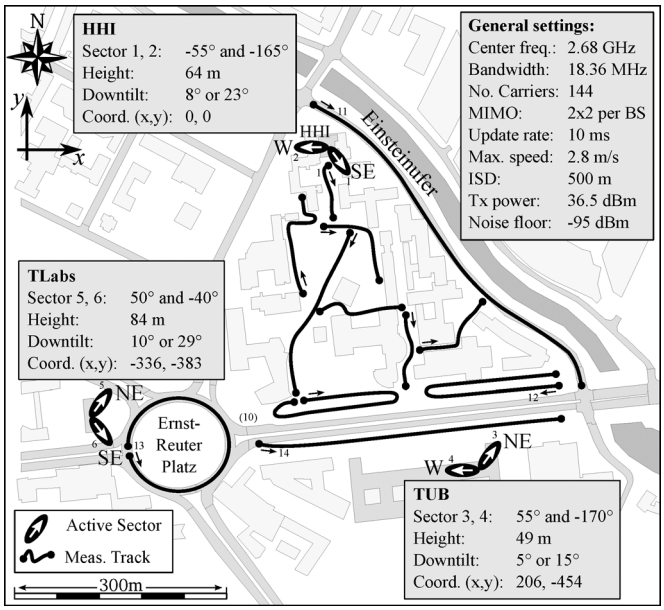

Fig. 5. Overview map of the measurement scenario.

packet stream as described in [28]. This data stream was tapped at the terminal and recorded to a notebook computer.

Custom import filters provide access to the stored CIRs. The import filters extract a $2 \times 12 \times 144$ channel tensor every 10 ms. The dimensions correspond to the number of Rx antennas, the total number of Tx antennas, and the number of samples in the frequency domain, respectively. We use the preprocessing technique described in [30] to extract the MPCs from the CIR. Essentially, the preprocessing estimates

$$\tilde{h}_n = \sum_{l=1}^{L} \underbrace{\alpha_l \cdot e^{j\phi_l}}_{=g_l} \cdot e^{-j2\pi \cdot \tau_l \cdot B \frac{n}{N}} \tag{39}$$

where α_l is the amplitude, ϕ_l is the phase, τ_l is the delay of the lth MPC, B is the measurement bandwidth of 18.36 MHz, and $n = 1 \ldots N$ is the index of the sample point in frequency domain. Due to the preprocessing, $\tilde{h}$ has an approximately 6 dB better signal-to-noise ratio (SNR) than the raw measurement data. Both the preprocessed data (39) and the output of the channel model (37) have the same format. Thus, identical routines can be used to obtain the LSPs.

Fig. 5 shows an overview of the measurement scenario, giving the coordinates and heights (in units of meters), the antenna orientations, and the downtilt settings for each BS site. Three BSs are located around the Ernst–Reuter–Platz in downtown Berlin, Germany. They are at the rooftop of the Heinrich Hertz Institute (HHI), the Deutsche Telekom Laboratories (TLabs) and the main building of the Technische Universität Berlin (TUB). The 12 measurement tracks with a total length of 3.1 km are plotted as thick black lines. The measurements were repeated twice with different downtilt settings. In the first setting, the main beam of the high-gain antenna reached the ground at 90% of the inter-site distance (ISD) (450 m). In the second setting, this distance was reduced to 33% of the ISD (170 m). In this way, different interference scenarios can be investigated.

TABLE II
PARAMETERS FOR THE URBAN MACRO-CELL (UMA) SCENARIO

Parameter		LOS			NLOS		
		WIN.	Berlin	Ref.	WIN.	Berlin	Ref.
No. Clusters	L	8	15		20	25	
Path Gain	A	2.60	2.10	own data	3.31	2.85	own data
	B	33.6	47.5	own data	38.8	38.0	own data
SF (dB)	σ	4.0	3.7	own data	8.0	4.0	own data
decorr. [m]	λ	45	90	own data	50	100	own data
Delay Spread	μ	-7.39	-6.69	own data	-6.63	-6.47	own data
($\log_{10}$s)	σ	0.63	0.30	own data	0.32	0.20	own data
decorr. [m]	λ	40	130	own data	40	100	own data
Delay factor	r_τ	2.5	2.5	[2]	2.3	2.0	[2], [1]
K-factor	μ	7.0	2.7	own data	N/A	-6.3	own data
(dB)	σ	3.0	2.3	own data	N/A	3.7	own data
decorr. [m]	λ	12	23	own data	N/A	40	own data
ASD	μ	1.00	0.65	[2], [18], [19]	0.93	0.65	[2], [18], [19]
($\log_{10}°$)	σ	0.25	0.23	[2], [18], [19]	0.22	0.22	[2], [18], [19]
decorr. [m]	λ	15	8	[2], [19]	50	25	[2], [19]
per cluster	c_ϕ	6	2	[2]	2	6	[2]
ESD	μ	0.70	0.70	[3]	0.90	0.90	[3]
($\log_{10}°$)	σ	0.20	0.20	[3]	0.20	0.20	[3]
decorr. [m]	λ	15	15	[3]	50	30	[3]
per cluster	c_ϕ	3	3	[3]	3	3	[3]
ASA	μ	1.70	1.61	[2], [18], [19]	1.72	1.50	[2], [18], [19], [17]
($\log_{10}°$)	σ	0.19	0.17	[2], [18], [19]	0.14	0.16	[2], [18], [19]
decorr. [m]	λ	15	11	[2], [19]	50	45	[2], [19], [17]
per cluster	c_ϕ	12	12	[2]	15	15	[2]
ESA	μ	0.95	1.16	[18], [19], [3]	1.26	1.25	[18], [19], [3]
($\log_{10}°$)	σ	0.16	0.14	[18], [19], [3]	0.16	0.14	[18], [19], [3]
decorr. [m]	λ	15	11	[19], [3]	50	25	[19], [3]
per cluster	c_ϕ	3	3	[3]	7	7	[3]
XPR	μ	8.00	9.00	[2], [19], [32]	7.00	7.75	[2], [19], [32]
(dB)	σ	4.00	4.30	[2], [19], [32]	3.00	4.30	[2], [19], [32]

B. Channel Model Setup

We imported the Tx-positions, sector orientations and Rx-tracks into the model and split the measurement tracks into 190 segments. Each segment has an average length (including the overlapping part) of 24 m with a standard deviation of 6 m. A separation into LOS and NLOS parts was done based on the overall received power and a 3-D model of downtown Berlin. We assume that there is no inter-site correlation of the LSPs due to the large ISD and the high angular separation at the MT [31]. However, inter-sector correlation at the same BS is included implicitly since we combine the antennas of different sectors into one array.

When parameterizing the model, we found some differences between our measurement results and the WINNER parameters. For example, many WINNER results (e.g., [2], [18], [19]) show median DS values of around 40 ns for LOS and 70–230 ns for NLOS. Measured results from the scenario with low downtilts (0.9 ISD), however, show larger DS values of 200 and 300 ns, respectively. This was also reported by other authors (e.g., [17], [1], [11]). We also observed lower KF values, i.e., we found strong echoes even if the direct component was present. In some cases, the power of those echoes could even exceed the LOS power. Therefore, we decided to adjust some parameters to increase the match with our testbed. After all, our intention is to show that the model creates channels with similar properties as real world data.

Table II lists the LSPs from the WINNER model [2], [3] (Urban macro-cell scenario), as well as parameters that we extracted from our own measurement data (Berlin scenario). Table III provides the cross-correlation values between the LSPs. The cross-correlation matrix must be positive definite to create correlated sequences, e.g., by Cholesky factorization.

TABLE III
CROSS-CORRELATION VALUES

Cross-correlation			LOS DS	K	SF	ASD	ASA	ESD	ESA
	DS	Berlin	1	−0.35	−0.62	0	0.2	−0.4	0
		WIN.	1	−0.4	−0.4	0.3	0.72	−0.46	0
	K	Berlin	−0.1	1	0.6	0	−0.2	0	−0.3
		WIN.	N/A	1	0.3	0.1	−0.2	0	0
	SF	Berlin	−0.65	0.12	1	−0.2	−0.4	0	−0.6
N		WIN.	−0.4	N/A	1	−0.5	−0.5	0	−0.74
L	ASD	Berlin	0.1	0	0	1	0.5	0.5	−0.3
O		WIN.	0.4	N/A	−0.44	1	0.3	0.4	0
S	ASA	Berlin	0	−0.2	−0.2	0.5	1	0	0.3
		WIN.	0.6	N/A	−0.3	0.4	1	0	0.4
	ESD	Berlin	−0.4	0	0	0.5	0	1	0
		WIN.	−0.5	N/A	0	0.34	0	1	0
	ESA	Berlin	−0.2	−0.2	−0.5	−0.3	0.3	0	1
		WIN.	0	N/A	−0.64	−0.34	0	0	1

This is not the case for the WINNER parameters. Hence, we did some minor adjustments to the parameters to make the matrix positive definite.[4]

To calculate the angular spreads, we need antenna arrays with a high spatial resolution, such as those used by [19], [33], and [34]. However, those antennas are not compatible with our testbed. We can only directly validate the values for DS, PG, SF, and KF. To fill the gaps we refer to measurements that we did together with our partners at the Ilmenau University of Technology using a different channel sounder [35]. Hence, Table II includes the averages of the results from measurement campaigns in Dresden, Germany [19], Ilmenau, Germany, [18] and the WINNER parameters.

We made sure by extensive testing and debugging that for each parameter in the tables, our implementation of the model produces exactly the same value in the output channel coefficients. However, the table is only valid for omnidirectional radiation patterns. We included high-gain BS-antennas by a measured 3-D pattern provided by Kathrein. It contains the radiated power versus azimuth and elevation angle for one polarization at a fixed electrical downtilt of 10°. We added mechanical tilts as described in [16] to obtain the same downtilts as for the measurements. We also approximated the polarization for the second port and the cross-polarization isolation between the ports. Since we had no 3-D pattern of the receive antenna, we approximated it by a dipole antenna. However, with those antennas, the LSPs extracted from the channel coefficients differ from the values in the table.

We had to remove the antenna-influence to parameterize the model with our own measurement results. This was done using an iterative method: First, we calculate the parameter (e.g., the DS) from the measured data[5], calculate the log-normal distribution, and obtain the median DS_μ and standard deviation (STD) DS_σ. We then run the model and calculate $\mathrm{DS}_\mu^{[\mathrm{model}]}$ and $\mathrm{DS}_\sigma^{[\mathrm{model}]}$ from the model output. However, due to the weighting by the antenna pattern, some clusters get more power and others get less. We observed that this increases the width of the distribution of the DS. In the next step, we adjust the values at the input of the channel model to account for this difference. We then repeat the procedure until the values $\mathrm{DS}_\mu^{[\mathrm{model}]}$, $\mathrm{DS}_\sigma^{[\mathrm{model}]}$ converge to DS_μ, DS_σ. The same is done for all other parameters marked with "own data" in Table II.

[4]The corrections for the LOS scenario are: ASD-DS from 0.4 to 0.3, ASA-DS from 0.8 to 0.72, ESA-SF from -0.8 to -0.72, and ESD-DS from -0.5 to -0.46. The corrections for the NLOS scenario are: ASD-SF from -0.6 to -0.44, ESA-SF from -0.8 to -0.64, ESD-ASD from 0.5 to 0.34, and ESA-ASD from -0.4 to -0.34.

[5]We use the scenario where the downtilt is set to maximize the gain at 90% of the ISD for this evaluation.

C. Estimation of Large-Scale Parameters

In the following, we describe how the LSPs are calculated from both, the measured data and the modeled channels. The parameters are calculated on a per-snapshot basis. However, small-scale fading can lead to strong fluctuations of a parameter even in subsequent snapshots. To remove the influence of small-scale fading, we average the results of the computations within a radius of 30λ or 3.3 m [31].

a) Effective Path Gain (PG): We estimate the PG from the data by summing up the power of all L paths and averaging over the n_t transmit and n_r receive antennas of the ith sector. The amplitude of a single MPC is represented by α:

$$P_i = \frac{1}{n_r n_t} \sum_{r=1}^{n_r} \sum_{t=1}^{n_t} \sum_{l=1}^{L} \alpha_{r,t,l,i}^2. \tag{40}$$

b) Delay Spread (DS): During preprocessing, MPCs are estimated from each MIMO sublink independently. To cope with measurement noise and estimation errors, we developed a method to match the paths from different sublinks. We split the delay axis into $\bar{L}$ intervals of 50-ns length[6] and add up the power of all MPCs from all links that fall into one interval. This also accounts for the jitter on the path delays of successive CIRs. The DS is then calculated as [36]

$$\sigma_{\tau i} = \sqrt{\frac{1}{P_i} \cdot \sum_{\bar{l}=1}^{\bar{L}} P_{\bar{l},i} \cdot \left(\tau_{\bar{l},i}\right)^2 - \left(\frac{1}{P_i} \cdot \sum_{\bar{l}=1}^{\bar{L}} P_{\bar{l},i} \cdot \tau_{\bar{l},i}\right)^2} \tag{41}$$

where the index $\bar{l}$ indicates the interval number, $P_{\bar{l}}$ is the sum-power of all paths falling into the $\bar{l}$th interval, $\tau_{\bar{l}}$ is the mean delay of the interval. We evaluated the performance of this approach[7] and found that at 5-dB SNR, the median error is 10%.[8] In 90% of the CIRs the error is below 35%, i.e., the estimated DS is at most 35% longer or shorter than the actual DS from the unprocessed, noise-free channels.

c) K-Factor (KF): The KF is defined as the ratio of the power of the direct path divided by the sum-power of all other paths. Some literature sources (e.g., [37] and [36]) define the KF with respect to the strongest path in the CIR which can originate from a dominant scatterer. In our model, however, the KF is

[6]The interval length corresponds to the time resolution of our measurement system, which is 54.5 ns at 18.36-MHz bandwidth.

[7]This evaluation was done by generating 2×2 cross-polarized MIMO channels with a known DS in the channel model. Then we transformed the output into the frequency-domain and added noise such that the SNR was 5 dB. Then we extracted the paths the same way, as we did for the measurements and calculated the DS from the preprocessed data.

[8]The percentage p is calculated by taking the actual value $\sigma_\tau^{[\mathrm{actual}]}$ and the estimated value $\sigma_\tau^{[\mathrm{est.}]}$ and calculating

$$p = \frac{\left|\sigma_\tau^{[\mathrm{actual}]} - \sigma_\tau^{[\mathrm{est.}]}\right|}{\sigma_\tau^{[\mathrm{actual}]}} \cdot 100.$$

defined as the power ratio between LOS and NLOS. Hence, to estimate the KF we have to detect the LOS path.

Our empirical detection of the LOS path works in three steps: First, we sum up the PDPs of all MIMO sublinks of one sector. Then we look for a peak at the beginning of this sum-PDP, i.e., we detect the first path that exceeds 1% of the total power. This ensures that noise at the beginning of the CIR is excluded. The noise also leads to jitter on the estimated delays from different sublinks. In order to account for this jitter, we try to match paths from all MIMO sublinks that have roughly the same delay as the peak detected in the first step. Therefore, in the second step, we look for the strongest path on each MIMO link separately within a 50-ns window before and after the peak delay. If the LOS path is correct, then its delay should not change significantly over a short distance. Thus, in the third step, we compare the LOS delays of successive snapshots within a 5-m radius and remove false detections. From the remaining snapshots, we calculate the KF as

$$K_i = \frac{P_i^{[\mathrm{LOS}]}}{P_i - P_i^{[\mathrm{LOS}]}}, \quad \text{where} \quad P_i^{[\mathrm{LOS}]} = \sum_{r=1}^{n_r}\sum_{t=1}^{n_t} P_{r,t,i}^{[\mathrm{LOS}]}. \tag{42}$$

Since the KF depends on the correct detection of the LOS path, there will be an error if this detection fails. We found that at 5-dB SNR, the median error is 1.4 dB (32%). The highest deviations occur in strong NLOS conditions. Here, the calculated values for the KF can be up to 5 dB higher than expected. For this reason, we evaluate the KF separately for the LOS segments of the measurement track where we can expect that our empirical estimator works well.

d) Large-Scale Parameter Correlations: For each 30 λ interval, we get values for the SF, the KF, and the DS. Roughly half of those values can be attributed to LOS and the other half to NLOS propagation. The decorrelation distance and the cross-correlation are calculated in the log-domain [38] using the Pearson product-moment correlation coefficient [39] where a_k and b_k contain K samples of a LSP, e.g., the DS, SF or KF along the measurement tracks:

$$\rho\{\mathbf{a},\mathbf{b}\} = \frac{\frac{1}{K}\sum_{k=1}^{K} a_k \cdot b_k^* - \frac{1}{K^2}\sum_{k=1}^{K} a_k \cdot \sum_{k=1}^{K} b_k^*}{\sqrt{\left(\sum_{k=1}^{K}\frac{|a_k^2|}{K} - \left|\sum_{k=1}^{K}\frac{a_k}{K}\right|^2\right)\left(\sum_{k=1}^{K}\frac{|b_k^2|}{K} - \left|\sum_{k=1}^{K}\frac{b_k}{K}\right|^2\right)}}. \tag{43}$$

For the decorrelation distance d_λ, we calculate $\rho\{\mathbf{a},\mathbf{a}^{(q)}\}$ where the superscript (q) denotes a shift of $\mathbf{a}$ by q entries. Two adjacent LSPs values are 30λ or 3.3 m apart from each other. Hence, for $q = 1$, we get the correlation coefficient at 3.3 m distance. For $q = 2$, we get it at 6.6 m distance. This is repeated for values up to $q = 12$ or 40 m distance. We then use those 12 values to fit an exponential function

$$\rho(d) = e^{-\frac{d}{d_\lambda}} \tag{44}$$

where both the distance d and the decorrelation distance d_λ are given in units of meters.

D. Estimation of Performance Metrics

a) Geometry Factor (GF): The geometry factor (GF) is a lower bound for the actual signal to interference and noise ratio (SINR). It is defined as the power ratio of the serving BS to all interfering BSs plus noise:

$$\mathrm{GF} = \frac{\mathrm{E}_{\mathrm{f/t}}[P_i]}{P^{[\mathrm{noise}]} + \sum_{\forall k, k\neq i} \mathrm{E}_{\mathrm{f/t}}[P_k]} \leq \mathrm{E}[\mathrm{SINR}_{\mathrm{inst.}}] \tag{45}$$

where $\mathrm{E}_{\mathrm{f/t}}[P]$ denotes the expectation value of the power over frequency and over the snapshots within a 30λ radius. This ensures that the effect of fast fading is removed. The noise power $P^{[\mathrm{noise}]}$ is limited either by thermal noise (-95 dBm) or by the sensitivity of the measurement system. Our system is based on commercial equipment that is optimized to achieve a SNR of 30 dB. For the modeled channels, we set $P^{[\mathrm{noise}]}$ accordingly to make the results comparable. Due to handover between cells, we always assign the MT to the sector with the highest received power.

b) Single-User Capacity at a Fixed SNR: We calculate the capacity C [40] measured in bps/Hz of the ith sector by

$$C_i^{[\mathrm{fixed}]} = \frac{1}{N}\sum_{n=1}^{N} \log_2 \det\left(\mathbf{I} + \frac{\sigma}{n_t \cdot P_i}\mathbf{H}_{n,i}\mathbf{H}_{n,i}^H\right) \tag{46}$$

where $\mathbf{I}$ is the 2×2 identity matrix. At a fixed SNR σ of 10 dB, the capacity depends only on the structure of the channel matrix $\mathbf{H}$ and the influence of the PG is removed. Values of $C_i^{[\mathrm{fixed}]}$ can be in between 4 bps/Hz for singular matrices and 6.9 bps/Hz for orthogonal matrices. We averaged the results within a 30 λ radius. The median error at 5–dB SNR comparing noise-free with noisy 2×2 keyhole channels [41] is 7.6% and does not exceed 10.7% in 90% of the cases.

c) Single-User Capacity With Inter-Cell Interference: We calculate the interference limited capacity using the quasistatic block flat-fading MIMO model [42] with

$$\mathbf{y}_n = \mathbf{H}_{n,i}\mathbf{x}_{n,i} + \sum_{\forall k, k\neq i} \mathbf{H}_{n,k}\mathbf{x}_{n,k} + \mathbf{v} \tag{47}$$

where $\mathbf{y}_n$ is the received signal vector on subcarrier n, $\mathbf{x}_n$ is the transmit data vector, $\mathbf{H}_{n,i}$ is the channel matrix for the serving sector i, and $\mathbf{v}$ is additive white Gaussian noise. Without channel knowledge at the Tx, the power is equally distributed over the transmit antennas. The capacity then notes

$$C_i = \frac{1}{N}\sum_{n=1}^{N} \log_2 \det\left(\mathbf{I} + \mathbf{Z}_{n,i}^{-1}\mathbf{H}_{n,i}\mathbf{H}_{n,i}^H\right), \tag{48}$$

$$\mathbf{Z}_{n,i} = P^{[\mathrm{noise}]} \cdot \mathbf{I} + \sum_{\forall k, k\neq i} \mathbf{H}_{n,k}\mathbf{H}_{n,k}^H, \tag{49}$$

where $\mathbf{Z}$ is the interference covariance matrix. Without interference, we set $P^{[\mathrm{noise}]} = (P_i \cdot n_t)/(\sigma)$ and get the same results as when using (46). However, here we use the noise power $P^{[\mathrm{noise}]}$ estimated from the measured channels. This value already includes the transmit power and the factor $1/n_t$. The median error at an average SNR of 5 dB is 1.8% and does not exceed 8.5% in 90% of the cases.

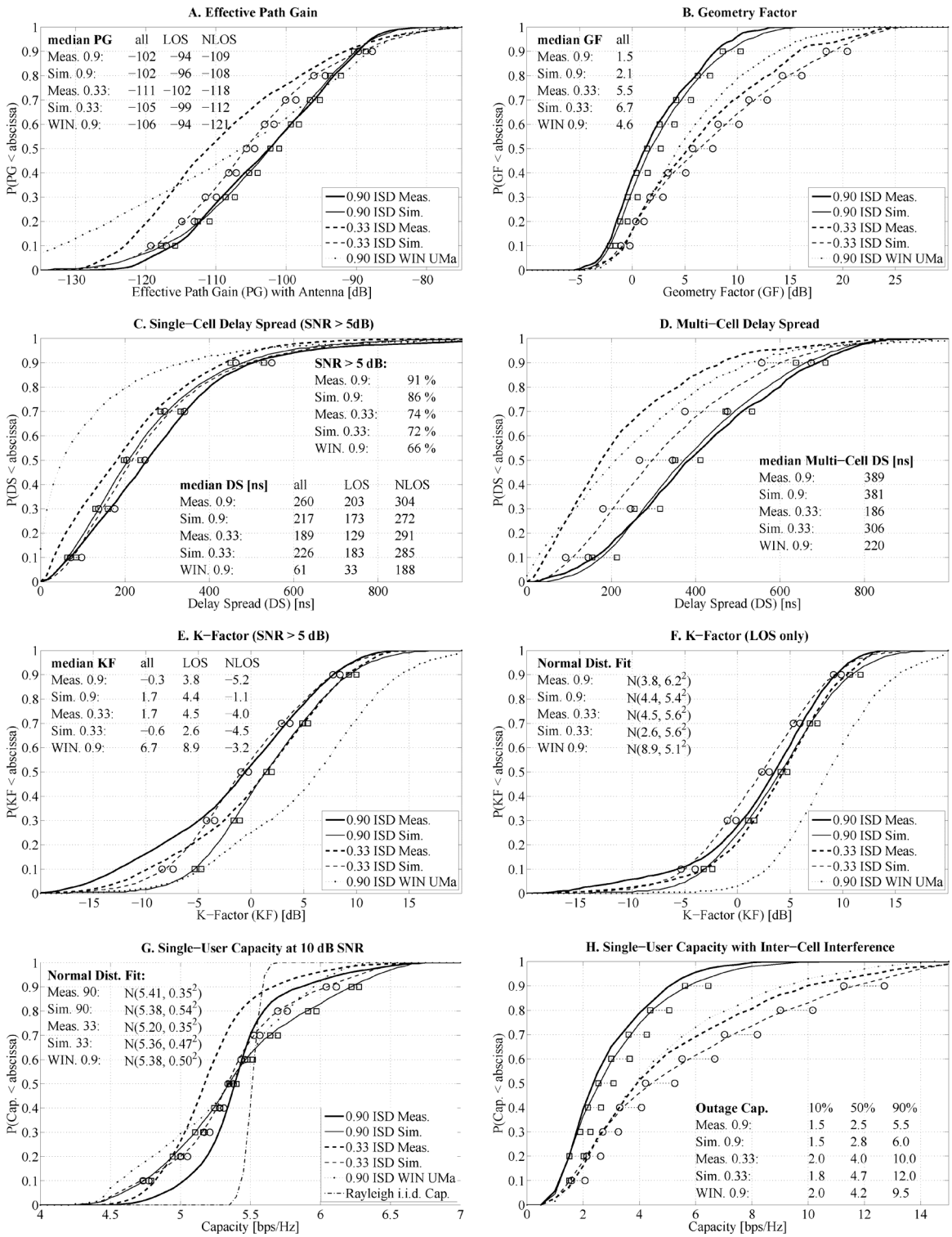

Fig. 6. Comparison of the distributions of several channel parameters. The thick lines are extracted from the measurements, the thin lines from the model. Solid lines are for the low downtilt (0.9 ISD), dashed lines for the high downtilt (0.33 ISD). The errorbars (dots around the modeled curves) indicate the standard deviation of the spread in the results when initializing the channel model 40 times with different random seeds. Squared endings are for the low downtilt and round endings for the high downtilt.

IV. Results and Discussion

Fig. 6 depicts the results. Each plot contains five cumulative distribution function (CDF) curves. The solid lines show the results for the scenario with low downtilt, i.e., the main beam reaches the ground at 0.9 ISD or 450 m. The dashed lines show the results for the high downtilt (0.33 ISD, 170 m). The thick lines are for the measurements, the thin lines for the model results. The dotted line shows the results obtained from using the WINNER parameters. For this curve, all new features (e.g., time evolution, drifting, geometric polarization, scenario transitions) were disabled, 3-D antenna patterns were included, and the main beam reaches the ground at 0.9 ISD.

The plots can be grouped into two categories: single-link parameters (PG, DS, KF, capacity at 10-dB SNR) and multi-link parameters (GF, multi-cell DS, and interference limited capacity). The model yields 928 values (3.1-km track divided by 3.3-m averaging distance) for each multi-link parameter, and 5568 values (928×6 sectors) for each single-link parameter. We repeated the simulation 40 times. Hence, we got 40 CDFs and 40 median values (2-quantile) for each parameter. The average of those 40 values is plotted in the point where the ordinate shows a value of 0.5. The STD above and below the mean of those 40 samples determines the width of the errorbar. Squared endings are for the low tilt (0.9 ISD) and round endings for the high downtilt (0.33 ISD). Generally, the results for the low downtilt agree better than for the high downtilt since we adjusted the model parameters in Table II for the low downtilt data.

A. Effective Path Gain

The effective PG combines the directional antenna gain, the SF, the distance-dependent PG, and the different propagation parameters for LOS and NLOS into one curve. The testbed results agree well for the low downtilts (0.9 ISD). However, there are differences at high downtilts. The NLOS parts have on average 6 dB more power in the modeled channels compared with the measured ones. The LOS part, on the other hand, has only 3 dB more power. A possible explanation is that at high downtilts most of the radiated power is localized in a small area. If the MT is close to one of those areas, the received power is dominated by the BS serving this area. In our measurement system, the achievable SNR is limited. Thus, weak clusters from links to other BSs often fall below the noise floor and cannot be resolved. The model, on the other hand, does not have this limitation.

The WINNER results show good agreement in the LOS scenario. However, the NLOS power is on average 12 dB lower than in our measurements. This can be explained by the high NLOS path loss coefficient of 3.31 in the WINNER parameters. In our measurements, we got a value of 2.85.

B. Geometry Factor

At higher downtilts (0.33 ISD), the coverage area of a sector is small and little power is radiated into the neighboring cells. Hence, the interference situation can be improved by increasing the downtilt. This is predicted well by the channel model when using our own parameterization. However, in this case the model predicts a GF that is roughly 1 dB better compared with the measurements. Two reasons could be behind this: First, the exact positions of the buildings on the campus are not included in the model. Thus, the effective path gain at the MT positions is different for each initialization of the model. Second, the synthetic antenna patterns in the model do not perfectly match the real ones in the measurement. This changes the GF, since the power distribution on the ground differs from the measurements.

The WINNER results show a 3 dB higher GF. This can also be explained by the high WINNER NLOS path loss coefficient. NLOS channels have significantly less power which increases the GF in cases when there is a LOS link to one of the BSs. We could confirm this by adjusting the NLOS path loss coefficients for the simulations to the values from our testbed. This reduced the difference from 3 dB to 1.5 dB.

C. Single-Cell Delay Spread

The DS in Fig. 6(C) depends on the KF and the LOS probability, which was 50% in our testbed. At low SNR, calculation of the DS becomes erroneous since many MPCs fall below the noise floor. Thus, we show only the results for areas where the SNR was at least 5 dB. This includes 90% of the low downtilt data and 75% of the high downtilt data.

An interesting observation is that the antennas have almost no influence on the DS. This becomes clear when comparing the DS from Table II with the DS in Fig. 6(C). The median LOS value from Table II (excluding antennas) is 200 ns. The corresponding values calculated from the model output are 173 ns for low and 183 ns for high downtilts. For NLOS channels, Table II predicts 340 ns and the model outputs are 272 ns and 285 ns, respectively. The same holds for the measured channels except for the LOS-DS at high downtilts, which is 50 ns shorter. This known effect comes from the thresholding used to remove the noise from the data [36]. In our measurement system the noise floor is 30 dB below the peak power in the multi-cell CIR. At high downtilts the power difference between the serving cell and interfering cells can easily exceed 20 dB due to the antenna gain. This leaves a dynamic range of only 10 dB for the detection of MPCs in the interfering links. NLOS channels often fall below the 5 dB limit and are sorted out, but many LOS channels seem to have a shorter DS because weak MPCs cannot be resolved. Modeled channels do not have this limitation and thus show a larger DS.

The results from the WINNER parameters show a significant difference. First, only 66% of the channels are above the 5-dB SNR limit. This is another consequence of the high NLOS path loss coefficient. Hence, most of the DS values in the distribution come from LOS channels which lowers the overall DS. Second, as we mentioned in Section III-B, many WINNER results (e.g., [2], [18], [19]) show too little values for the DS, whereas other literature sources (e.g., [17], [1], [11]) confirm our results.

D. Multi-Cell Delay Spread

The multi-cell DS [Fig. 6(D)] is calculated from the combined PDP of all BSs. Hence, it includes the different mean-delays. This is important if a MT is connected to several BSs at the same time, e.g., when using soft handover or joint transmission. For the low downtilts, the measurement and model results agree perfectly. The median DS almost doubles compared with single-cell transmission, but the maximum delay spread does not increase. The results for the high downtilts, however, differ significantly. The reason is likely to be the same as discussed above: Our measurement setup cannot resolve sufficient MPCs if the power difference between serving and interfering links is high.

As for the WINNER results, the low single-cell DS is also reflected in the multi-cell DS. Values from the model are roughly 40% smaller than in the measured channels.

E. K-Factor

The KF [Fig. 6(E)] is influenced by the LOS probability and the antenna gain. As for the DS, we limited the evaluation to areas where the SNR was at least 5 dB. In the model, lower downtilts (0.9 ISD) result in a 2.3 dB higher KF compared with the data set with high downtilts. This is reasonable, because at high downtilts the beam of the high-gain antenna illuminates only a small area close to the BS. The KF is reduced in all other areas because the direct component is attenuated. In the measured data, on the other hand, high downtilts result in a better KF. However, this can also be explained by the missing MPCs due to the reduced resolution of our measurement system.

The WINNER parameters show high values for the KF (see Table II). This explains the low values for the DS. When the KF is high, the DS is short since more energy is concentrated on the direct path. The WINNER model also includes no KF modeling for NLOS channels. In this case, our estimation method uses the first cluster that exceeds 1% of the total power as the direct one. Even then, however, the estimated KF from the modeled channels is 7 dB higher than in the measurements.

F. K-Factor (LOS Only)

If the KF is small, the detection of the LOS cluster might fail because a later, stronger cluster may be taken as the first one by accident. For this reason, in Fig. 6(F), we limited the evaluation to areas where there is a LOS connection between Tx and Rx. Here, the match between the four curves is better, especially in the scenario with low downtilts (0.9 ISD) where the curves almost agree perfectly.

The effect of the high-gain antennas on the KF can be seen when comparing the parameters in Table II with the results in Fig. 6(F). The LOS-KF in Table II follows a normal distribution with $\mathcal{N}(2.7, 2.3^2)$ for our own parameterization and $\mathcal{N}(7, 3^2)$ for the WINNER scenario. The inserted text in the figure gives the fitted parameters $\mathcal{N}(\mu, \sigma^2)$ for the empirical results. In some areas the weighting by the antenna pattern amplifies the direct component, and the KF increases. In other areas, outside the cell, the direct component is attenuated, and the KF decreases. This explains the larger spread in the empirical distributions.

G. Single-User Capacity at a 10-dB SNR

The capacity [Fig. 6(G)] depends on all the channel parameters and the antennas. We limited the evaluation to areas where the SNR in the data was at least 5 dB. We also plotted the distribution of an i.i.d. channel for comparison. There are significant fluctuations in all the results. Clearly, it is important to adjust the transmission mode to the channel rank [43].

The median capacity of 5.3 bps/Hz is predicted well by the channel model. However, the width of the modeled distributions is wider compared with the measurements. A reason for this could be discrepancies in the values for the angular spreads. However, it is difficult to quantify this influence without access to accurate angular spread measures. It is also possible that our measurement system causes some random phase fluctuations within different MIMO sublinks due to the over-the-air synchronization. Such a random component would explain the steeper distribution of the measurement results.

TABLE IV
MEASURED AND SIMULATED VALUES DECORRELATION DISTANCE AND CROSS-CORRELATION VALUES

Scen.	Parameter	Meas. value	Model setup	Model output AVG	Model output STD	WIN. UMa
LOS	SF Decorr. Dist. [m]	156	90	178	28	45
	DS Decorr. Dist. [m]	78	130	61	15	40
	KF Decorr. Dist. [m]	39	23	36	5	12
	DS-KF Cross-corr.	-0.49	-0.35	-0.56	0.11	-0.40
	DS-SF Cross-corr.	-0.65	-0.62	-0.42	0.13	-0.40
	KF-SF Cross-corr.	0.45	0.60	0.45	0.04	0.30
NLOS	SF Decorr. Dist. [m]	142	100	134	21	50
	DS Decorr. Dist. [m]	56	100	58	13	40
	KF Decorr. Dist. [m]	41	40	35	6	N/A
	DS-KF Cross-corr.	-0.33	-0.10	-0.48	0.08	N/A
	DS-SF Cross-corr.	-0.64	-0.65	-0.33	0.08	-0.40
	KF-SF Cross-corr.	0.19	0.12	0.38	0.05	N/A

We need a higher number of antennas and synchronized receivers to correctly validate the capacity distribution. This would provide more insight into the spatial structure of the channel and allow us to calculate the angular spreads, e.g., by using the method from [31]. However, such additional measurements are beyond the scope of this paper.

H. Single-User Capacity With Inter-Cell Interference

The distribution of the interference limited capacity is plotted in Fig. 6(H). The inserted text shows the outage capacity for each curve. In general, the simulations with our own parameterization tend to predict a slightly higher capacity. However, this is consistent with the geometry factors [Fig. 6(B)] which are also slightly higher. The simulations from the WINNER parameters, however, predict a 60% higher capacity.

I. LSP Correlations

Table IV summarizes the results for the decorrelation distance and cross-correlation. It contains the values obtained from the measured channels (Meas. value), the parameterization of the channel model (Model setup), and the calculated values from the model output. The average (AVG) and the standard deviation (STD) result from the 40 repetitions of the simulations. The last column contains the values from the WINNER urban macro-cell scenario [2].

The effect of the high-gain antennas can be seen when comparing the model setup with the model output. In both scenarios (LOS and NLOS) the decorrelation distance increases for the SF and decreases for the DS. The values for the KF increase only in the LOS scenario. The cross-correlations DS-KF and KF-SF are in good agreement for LOS. For both scenarios, however, the model output for DS-SF is significantly lower. This indicates that the true cross-correlation between DS and SF might even be smaller than -0.6, but that would destroy the positive definiteness of the cross-correlation matrix. The NLOS cross-correlations DS-KF and KF-SF show significant differences when measurements, model setup, and model output are compared. This can be attributed to the fact that KF estimation is very inaccurate when the KF is below 0 dB. The decorrelation distances from the WINNER model are only half as big as in our setup. However, our results agree very well with [38].

V. Conclusion

In this paper, we extended the popular WINNER channel model with new features that allow the generation of channel traces with temporal evolution. The new model supports freely configurable network layouts with multiple transmitters and receivers, and it is scalable from single-link single-antenna systems to heterogeneous multi-link MIMO scenarios. We further improved the model by merging the methods for calculating LOS and NLOS channels (WINNER uses different methods) and by implementing a new polarization model.

We validated the evolved model by measurements in a relevant scenario, i.e., by using BS positions and antennas that are realistic for a commercial setup. All evaluated parameters, for both single-link and multi-link setups, are in good agreement. We have shown that it is possible to generate channel traces with similar characteristics as measured data. This will speed up the evaluation of new algorithms, since we can now obtain realistic performance results in an early stage of development. All existing WINNER parameter tables can be used. Hence, the new model allows us to perform virtual field trials in many scenarios. We performed simulations with the original WINNER parameters and compared the results with our findings. There were some differences. Due to this, we would suggest carefully checking the WINNER parameter tables against real-world scenarios. However, this would exceed the scope of this paper.

Further extensions can be made regarding the generation of departure and arrival angles. Currently, azimuth and elevation angles are calculated independently (see Section II-C). It might be preferable to extract both angles from a bivariate distribution. This is expected to yield better results if the elevation of some paths is close to $\pm 90^\circ$. Another improvement could be made by including the cluster model from Czink and Oestges [44]. This would allow the tracking of departure angles for different positions of the Tx-antenna. However, how to generate the departure angles of the so-called "twin cluster" in order to achieve a given power angular spectrum is still an open issue. In the COST model, which also uses this approach, the angular dependency of the power is not considered. How the published findings on the birth/death probability of individual scattering clusters [13], [14] can be mapped to the temporal evolution of the LSPs is also an open issue. For example, randomly creating and removing paths as suggested by [12] would significantly alter the delay and angular spread. Finally, inter-site correlations of the LSPs can be included by incorporating more advanced algorithms [45], [46], [21] for generating the parameter maps for the initial parameters.

Appendix A

The correction function $C_\phi(L, K)$ takes the influence of the KF and the varying number of clusters on the angular spread into account. To approximate the function, we generate the angles using (10) to (13) with the correction function set to $C = 1$. Then we calculate the spread $\tilde{\sigma}_\phi$ as proposed in [36]:

$$\tilde{\sigma}_\phi = 2\pi \cdot \sqrt{1 - \frac{|F_1|^2}{F_0^2}},$$

$$F_n = \sum_{l=1}^{L} P_l \cdot \exp(-j \cdot \phi_l \cdot n) \tag{50}$$

where ϕ_l is the angle calculated by (13), and F_n is the nth complex Fourier coefficient. The correction function now follows from comparing $\tilde{\sigma}_\phi$ with σ_ϕ. However, two aspects need to be considered:

1) Due to the randomization of the angles in (11), we have to take the average angle over a sufficiently large quantity (≈ 1000 realizations) of $\tilde{\sigma}_\phi$. This value is denoted as $\bar{\sigma}_\phi$.
2) There is a nonlinear relationship between the angular spread in the simulated data $\bar{\sigma}_\phi$ on the initial value σ_ϕ. This comes from the logarithm in (10) and the modulo in (12). However, for small values, the relationship can be approximated by a linear function. We define the maximum angular spread $\sigma_\phi^{\max}$ as the point where the error between the corrected value $(\sigma_\phi)/(C_\phi(L, K))$ and $\bar{\sigma}_\phi$ is 10°.

For a range of typical values $L \in [2, 42]$ and $K_{[\mathrm{dB}]} \in [-20, 20]$, we numerically calculate $C_\phi(L, K)$ by

$$C_\phi(L, K) = \frac{1}{\sigma_\phi^{\max}} \cdot \int_0^{\sigma_\phi^{\max}} \frac{\bar{\sigma}_\phi(\sigma_\phi)}{\sigma_\phi} d\sigma_\phi \tag{51}$$

where the σ_ϕ-dependency of $\bar{\sigma}_\phi(\sigma_\phi)$ comes from the individual angles ϕ_l.

Acknowledgment

The authors would like to thank V. Jungnickel, A. Forck, F. Bauermeister, S. Schiffermueller, S. Schubert, S. Wahls, T. Haustein [Heinrich Hertz Institute (HHI), Berlin, Germany], W. Kreher, J. Mueller, H. Droste, G. Kadel [Deutsche Telekom AG, T-Labs, Darmstadt, Germany], and V. Braun [Alcatel-Lucent Bell Labs, Stuttgart, Germany] for their help with setting up the testbed and assistance during the measurements. They would also like to thank G. Sommerkorn, C. Schneider, M. Kaeske [Ilmenau University of Technology (IUT), Ilmenau, Germany], E. Eberlein and F. Burkhardt [Fraunhofer IIS, Erlangen, Germany] for the fruitful discussions on the QuaDRiGa channel model and the manuscript of this paper.

References

[1] "Spatial channel model for multiple input multiple output (MIMO) simulations," Tech. Rep., 3, 2011, 3GPP TR 25.996 v10.0.0.

[2] P. Kyösti *et al.*, "IST-4-027756 WINNER II D1.1.2 v.1.1: WINNER II Channel Models," Tech. Rep., 2007 [Online]. Available: http://www.ist-winner.org

[3] P. Heino *et al.*, "CELTIC/CP5-026 D5.3: WINNER+ final channel models," Tech. Rep., 2010 [Online]. Available: http://projects.celtic-initiative.org/winner+

[4] *Mobile Broadband Multimedia Networks*, L. Correia, Ed.. Amsterdam, The Netherlands: Elsevier, 2006, ch. 6.8, pp. 364–383, The COST 273 MIMO channel model.

[5] C. Oestges *et al.*, "Radio Channel Modeling for 4G Networks," in *Pervasive Mobile and Ambient Wireless Communications (COST Action 2100)*. New York, NY, USA: Springer, 2012, ch. 3, pp. 67–147.

[6] H. Xiao, A. Burr, and L. Song, "A time-variant wideband spatial channel model based on the 3 GPP model," in *Proc. IEEE VCT'06 Fall*, 2006, pp. 1–5.

[7] D. Baum, J. Hansen, and J. Salo, "An interim channel model for beyond-3G systems," in *Proc. IEEE VCT'05 Spring*, 2005, vol. 5, pp. 3132–3136.

[8] M. Shafi, M. Zhang, A. Moustakas, P. Smith, A. Molisch, F. Tufvesson, and S. Simon, "Polarized MIMO channels in 3-D: Models, measurements and mutual information," *IEEE J. Sel. Areas Commun.*, vol. 24, no. 3, pp. 514–527, Mar. 2006.

[9] A. Zajic, G. Stuber, T. Pratt, and S. Nguyen, "Wideband MIMO mobile-to-mobile channels: Geometry-based statistical modeling with experimental verification," *IEEE Trans. Veh. Technol.*, vol. 58, no. 2, pp. 517–534, Feb. 2009.

[10] J. Poutanen, K. Haneda, L. Liu, C. Oestges, F. Tufvesson, and P. Vainikainen, "Parameterization of the COST 2100 MIMO channel model in indoor scenarios," in *Proc. EUCAP'11*, 2011, pp. 3606–3610.

[11] M. Zhu, F. Tufvesson, and G. Eriksson, "The COST 2100 channel model: Parameterization and validation based on outdoor MIMO measurements at 300 MHz," Lund Univ., Lund, Sweden, Tech. Rep., 2012.

[12] N. Czink, T. Zemen, J.-P. Nuutinen, J. Ylitalo, and E. Bonek, "A time-variant MIMO channel model directly parametrised from measurements," *EURASIP J. Wireless Commun. Netw.*, 2009 [Online]. Available: http://jwcn.eurasipjournals.com/content/2009/1/687238

[13] K. Saito, K. Kitao, T. Imai, Y. Okano, and S. Miura, "The modeling method of time-correlated MIMO channels using the particle filter," in *Proc. IEEE VCT'11 Spring*, 2011, pp. 1–5.

[14] W. Wang, T. Jost, U. Fiebig, and W. Koch, "Time-variant channel modeling with application to mobile radio based positioning," in *Proc. IEEE GLOBECOM'12*, 2012, pp. 5038–5043.

[15] [Online]. Available: http://www.quadriga-channel-model.de

[16] S. Jaeckel, K. Börner, L. Thiele, and V. Jungnickel, "A geometric polarization rotation model for the 3-D spatial channel model," *IEEE Trans. Antennas Propag.*, vol. 60, no. 12, pp. 5966–5977, Dec. 2012.

[17] A. Algans, K. Pedersen, and P. Mogensen, "Experimental analysis of the joint statistical properties of azimuth spread, delay spread, and shadow fading," *IEEE J. Sel. Areas Commun.*, vol. 20, no. 3, pp. 523–531, Mar. 2002.

[18] C. Schneider, M. Narandzic, M. Käske, G. Sommerkorn, and R. Thomä, "Large scale parameter for the WINNER II channel model at 2.53 GHz in urban macro cell," in *Proc. IEEE VTC'10 Spring*, 2010, pp. 1–5.

[19] M. Narandzic, C. Schneider, M. Käske, S. Jaeckel, G. Sommerkorn, and R. Thomä, "Large-scale parameters of wideband MIMO channel in urban multi-cell scenario," presented at the EUCAP'11, 2011.

[20] K. Bakowski and K. Wesolowski, "Change the channel," *IEEE Veh. Technol. Mag.*, vol. 6, no. 2, pp. 82–91, Jun. 2011.

[21] S. Szyszkowicz, H. Yanikomeroglu, and J. Thompson, "On the feasibility of wireless shadowing correlation models," *IEEE Trans. Veh. Technol.*, vol. 59, no. 9, pp. 4222–4236, Sep. 2010.

[22] K. Pedersen, P. Mogensen, and B. Fleury, "Power azimuth spectrum in outdoor environments," *Electron. Lett.*, vol. 33, no. 18, pp. 1583–1584, 1997.

[23] M. Narandzic, M. Käske, C. Schneider, M. Milojevic, M. Landmann, G. Sommerkorn, and R. Thomä, "3D-antenna array model for IST-WINNER channel simulations," in *Proc. IEEE VTC'07 Spring*, 2007, pp. 319–323.

[24] M. Hata, "Empirical formula for propagation loss in land mobile radio services," *IEEE Trans. Veh. Technol.*, vol. VT-29, no. 3, pp. 317–325, Aug. 1980.

[25] V. Jungnickel *et al.*, "Demonstration of virtual MIMO in the uplink," presented at the IET Smart Antenna Coop. Commun. Seminar, London, U.K., Oct. 2007.

[26] V. Jungnickel *et al.*, "Interference aware scheduling in the multiuser MIMO-OFDM downlink," *IEEE Commun. Mag.*, vol. 47, no. 6, pp. 56–66, Jun. 2009.

[27] V. Jungnickel *et al.*, "Coordinated multipoint trials in the downlink," in *Proc. IEEE Globecom Workshops'09*, 2009, pp. 1–7.

[28] V. Jungnickel *et al.*, "Field trials using coordinated multi-point transmission in the downlink," in *Proc. IEEE PIMRC'10 WDN-Workshop*, 2010, pp. 440–445.

[29] V. Jungnickel, K. Manolakis, L. Thiele, T. Wirth, and T. Haustein, "Handover sequences for interference-aware transmission in multicell MIMO networks," presented at the WSA'09, Berlin, Germany, Feb. 16–18, 2009.

[30] S. Jaeckel, L. Thiele, and V. Jungnickel, "Interference limited MIMO measurements," in *Proc. IEEE VTC'10 Spring*, 2010, pp. 1–5.

[31] N. Jaldén, P. Zetterberg, B. Ottersten, and L. Garcia, "Inter-and intrasite correlations of large-scale parameters from macrocellular measurements at 1800 MHz," *EURASIP J. Wireless Commun. Netw.*, no. 3, 2007 [Online]. Available: http://jwcn.eurasipjournals.com/content/2007/1/025757

[32] L. Materum, J. Takada, I. Ida, and Y. Oishi, "Mobile station spatiotemporal multipath clustering of an estimated wideband MIMO doubledirectional channel of a small urban 4.5 GHz macrocell," *EURASIP J. Wireless Commun. Netw.*, 2009 [Online]. Available: http://jwcn.eurasipjournals.com/content/2009/1/804021

[33] M. Narandzic, M. Käske, S. Jäckel, G. Sommerkorn, C. Schneider, and R. S. Thomä, "Variation of estimated large-scale MIMO channel properties between repeated measurements," in *Proc. IEEE VTC'11 Spring*, 2011, pp. 1–5.

[34] S. Jaeckel, L. Thiele, A. Brylka, L. Jiang, and V. Jungnickel, "Intercell interference measured in urban areas," in *Proc. IEEE ICC'09*, 2009, pp. 1–6.

[35] R. Thomä, D. Hampicke, A. Richter, G. Sommerkorn, and U. Trautwein, "MIMO vector channel sounder measurement for smart antenna system evaluation," *Eur. Trans. Telecomm.*, vol. 12, pp. 427–438, 2001.

[36] T. Rappaport, *Wireless Communications. Principles and Practice*, 2nd ed. Upper Saddle River, NJ, USA: Prentice-Hall, 2002.

[37] L. Greenstein, D. Michelson, and V. Erceg, "Moment-method estimation of the Ricean k-factor," *IEEE Commun. Lett.*, vol. 3, no. 6, pp. 175–176, Jun. 1999.

[38] M. Zhu, F. Tufvesson, and J. Medbo, "Correlation properties of large scale parameters from 2.66 GHz multi-site macro cell measurements," in *Proc. IEEE VTC'11 Spring*, 2011, pp. 1–5.

[39] J. L. Rodgers and W. A. Nicewander, "Thirteen ways to look at the correlation coefficient," *Amer. Statist.*, vol. 42, pp. 59–66, 1988.

[40] I. E. Telatar, "Capacity of multi-antenna Gaussian channels," *Europ. Trans. Telecomm.*, vol. 10, no. 6, pp. 585–596, 1999.

[41] D. Chizhik, G. Foschini, and M. Gans, "Keyholes, correlations and capacities of multielement transmit and receive antennas," *IEEE Trans. Wireless Commun.*, vol. 1, pp. 361–368, Apr. 2002.

[42] E. A. Jorswieck and H. Boche, "Performance analysis of capacity of MIMO systems under multiuser interference based on worst-case noise behavior," *EURASIP J. Wireless Commun. Netw.*, vol. 2, pp. 273–285, 2004.

[43] M. Schellmann, L. Thiele, T. Haustein, and V. Jungnickel, "Spatial transmission mode switching in multi-user MIMO-OFDM systems with user fairness," *IEEE Trans. Veh. Technol.*, vol. 59, no. 1, pp. 235–247, Jan. 2010.

[44] N. Czink and C. Oestges, "The COST 273 MIMO channel model: Three kinds of clusters," in *Proc. IEEE ISSSTA'08*, 2008, pp. 282–286.

[45] T. Klingenbrunn and P. Mogensen, "Modelling cross-correlated shadowing in network simulations," in *Proc. IEEE VTC'99 Fall*, 1999, vol. 3, pp. 1407–1411.

[46] X. Cai and G. B. Giannakis, "A two-dimensional channel simulation model for shadowing processes," *IEEE Trans. Veh. Technol.*, vol. 52, no. 6, pp. 1558–1567, Nov. 2003.

Stephan Jaeckel (S'10–M'12) was born in Freiberg, Germany, in 1982. He received the B.Eng. and M.Eng. degrees in information and communications technology from Hochschule für Telekommunikation, Leipzig, Germany, in 2005 and 2007, respectively. He is currently working toward the Dr. Ing. (Ph.D.) degree in electrical engineering at Ilmenau University of Technology (IUT), Ilmenau, Germany.

In 2006, he was a summer student at CERN, Geneva, Switzerland, where he worked on the software for the LHCb particle detector. In 2007, he joined the Fraunhofer Heinrich

Hertz Institute, Berlin, Germany, where he worked on the measurement-based performance analysis of cooperative mobile communication systems. His current research interests include measurements and data analysis in heterogeneous multi-cell networks including relays as well as channel modeling for terrestrial and satellite systems.

Leszek Raschkowski was born in Pietersburg, South Africa, in 1983. He received the Dipl.-Ing. (M.S.) degree in electrical engineering in 2012 from Technische Universität Berlin, Germany.

Currently, he is a Research Associate at Fraunhofer Heinrich Hertz Institute, Berlin, Germany. His research interests include modeling and simulating radio propagation channels, as well as performance analysis of wireless communication systems.

Kai Börner (S'12) received the Dipl.-Ing. (M.S.) degree in electrical engineering in 2009 from the Technische Universität Berlin, Berlin, Germany, where he is currently working toward the Dr.-Ing. (Ph.D.) degree in electrical engineering.

He joined the Fraunhofer Heinrich Hertz Institute (HHI) in April 2009. His research interests lie in channel modeling, energy-efficient transmission, and self-organization in heterogeneous multiple-input multiple-output (MIMO) orthogonal frequency-division (OFDM)-based networks.

Lars Thiele (S'06–M'09) received the Dipl.-Ing. (M.S.) degree in electrical engineering from the Technische Universität Berlin, Berlin, Germany, in 2005 and the Dr.-Ing. (Ph.D.) degree from the Technical University of Munich (TUM), Munich, Germany, in 2013.

He joined the Fraunhofer Heinrich Hertz Institute (HHI), Berlin, Germany, in September 2005. He has contributed to receiver and transmitter optimization under limited feedback, performance analysis for multiple-input multiple-output (MIMO) transmission in cellular orthogonal frequency-division multiplexing (OFDM) systems, fair-resource allocation, and cooperative multipoint (CoMP) transmission under constrained channel state information at the transmitter (CSIT). He has authored and coauthored about 50 conference and journal papers as well as a couple of book chapters in the area of mobile communications. He leads the System Level Innovation research group at Fraunhofer HHI and is actively participating in the GreenTouch consortium.